

# High-Spatial Resolution Imaging Combining High-Order Adaptive Optics, Frame Selection, and Speckle Masking Reconstruction

Carsten Denker, Dulce Mascarinas, Yan Xu, Wenda Cao, Guo Yang, Haimin Wang and Philip R. Goode

*New Jersey Institute of Technology, Center for Solar-Terrestrial Research  
323 Martin Luther King Blvd, Newark, NJ 07102*

Thomas Rimmele

*National Solar Observatory, Sacramento Peak Observatory  
P.O. Box 62, Sunspot, NM 88349-0062*

March 6, 2004

**Abstract.** We present, for the first time, high-spatial resolution observations combining high-order adaptive optics (AO), frame selection, and post-facto image correction via speckle masking. The data analysis is based on observations of solar active region NOAA 10486 taken with the Dunn Solar Telescope (DST) at the Sacramento Peak Observatory (SPO) of the National Solar Observatory (NSO) on 2003 October 29. The high Strehl-ratio encountered in AO corrected short-exposure images provides highly improved signal-to-noise ratios leading to a superior recovery of the object's Fourier phases. This allows reliable detection of small-scale solar features near the diffraction limit of the telescope. Speckle masking imaging provides access to high-order wavefront aberrations, which predominantly originate at high atmospheric layers and are only partially corrected by the high-order AO system. In addition, the observations provided qualitative measures of the image correction away from the lock point of the AO system. We further present a brief inspection of the underlying imaging theory discussing the limitations and prospects of this multi-faceted image reconstruction approach in terms of the recovery of spatial information, photometric accuracy, and spectroscopic applications.

**Keywords:** Frame Selection, Adaptive Optics, Speckle Masking Method

## 1. Introduction

To advance our understanding of small-scale magnetic fields, higher light gathering capacity and spatial resolution are essential. This led to several initiatives for a new generation of solar telescopes with 1-meter apertures and beyond. These efforts include the 1-meter New Swedish Solar Telescope (NSST), which is already operational (Scharmer *et al.*, 2003); the German 1.5-meter GREGOR telescope (Volkmer *et al.*, 2003) and the 1.6-meter New Solar Telescope (NST) at Big Bear Solar Observatory (BBSO, Goode *et al.*, 2003), which are currently under construction; and the 4-meter Advanced Technology Solar Telescope (ATST) under NSO stewardship, which approaches the end of its design and development phase (Keil *et al.*, 2003).

This new or next generation of solar telescopes can only achieve its potential by relying on extensive use of in situ and/or post-facto image correction. Correlation tracking, spot tracking, and AO systems belong into the aforementioned class, while blind deconvolution algorithms, (speckle) phase diversity techniques, speckle de-

convolution, speckle holography, speckle masking method, etc. comprise the latter. The next steps in image reconstruction can be separated in two categories: (1) implementing post-facto techniques on parallel processors pushing image reconstruction toward real-time applications (e.g., Denker, Yang, and Wang, 2001) and (2) effectively combining in situ and post-facto image correction. An excellent example of the latter case has been presented by Scharmer *et al.* (2002), who used a *low-order* AO system with 15 corrected modes, frame selection, and an implementation of the phase diversity technique at the NSST to study sunspot fine structure with a resolution of about  $0.12''$ . Here, however, we present a more qualitative approach based on data obtained with a *high-order* AO system, frame selection, and speckle masking imaging.

The science target of our study was solar active region NOAA 10486, which has been one of the surprises of the declining phase of solar cycle 23. NOAA 10486 and its companions NOAA 10484 and 10488, which were all naked-eye sunspot groups, were responsible for major flare activity including several X-class flares. This activity culminated in an X28 flare on 2003 November 4, the largest X-ray flare in recorded history. The scientific results of the observing run will be presented in a forthcoming paper (Xu *et al.*, 2004). In the following sections, we present and discuss the image reconstruction procedure, where we “scrupulously” applied the speckle masking method (Weigelt, 1977; Weigelt and Wirtitzer, 1983; Lohmann, Weigelt, and Wirtitzer, 1983; de Boer, 1993) to AO corrected images, before scrutinizing the underlying assumptions, limitations, and prospects in the final section “Discussion and Conclusions”.

## 2. Adaptive Optics

The 76 cm entrance aperture of the DST is located about 40 m above ground to mitigate the effects of boundary layers seeing and the entire light path is evacuated until the light reaches the high-order AO system (Rimmele, 2000; Rimmele *et al.*, 2003) at the observing room to avoid internal telescope seeing. The effective focal length of the  $f/72$  system is about  $f_{\text{eff}} = 55$  m. The high-order AO system at NSO/SPO is also the prototype for a twin-system at BBSO (Ren *et al.*, 2003; Didkovsky *et al.*, 2003). Both AO systems will be used in dedicated observing runs as important building blocks to develop multi-conjugate AO for solar observations.

A tip/tilt mirror precedes the AO system to preserve the dynamic range of the 77 mm diameter, 97 actuator, deformable mirror to efficiently correct the high-order wavefront aberrations. The high-order wavefront aberrations are detected by a Shack-Hartman wavefront sensor from slope measurements derived from 76 sub-apertures, which are recorded on  $200 \times 200$  pixel of a custom built Complex Metal Oxide Semiconductor (CMOS) camera (Richards *et al.*, 2004). The data acquisition rate is 2.5 kHz. The closed loop bandwidth of the system is about 130 Hz (0 dB

crossover). The high order AO system has achieved Strehl ratios in excess of 0.7 (Langlois, Rimmele, and Moretto, 2004).

The maximum field-of-view (FOV) for science observations of the high-order AO system is about  $180'' \times 180''$ . The AO corrected data were acquired in two distinct science channels: (1) near-infrared (NIR) filtergrams at  $\lambda = 1,560 \pm 5$  nm were obtained with a high-speed ( $30 \text{ frames s}^{-1}$ ), large-format ( $1,024 \times 1,024$  pixel, FOV:  $91'' \times 91''$ ), low-noise ( $> 60\%$  quantum efficiency, 14-bit digitization,  $> 70$  dB dynamic range) Hg Cd Te/ $\text{Al}_2\text{O}_3$  CMOS camera based on a TCM 8600 sensor manufactured by Rockwell Scientific Imaging and (2) broad-band, short-exposure images “specklegrams” were obtained in the green continuum. This science data will be presented in a separate paper (Xu *et al.*, 2004).

### 3. Frame Selection

The 4 ms short-exposure images were obtained with a  $1,024 \times 1,024$  pixel 1M15 CCD camera manufactured by Dalsa. This high-speed, large-format CCD camera is usually used with the real-time image reconstruction (RTIR) system at BBSO (Denker, Yang, and Wang, 2001), which can reconstruct  $1,024 \times 1,024$  pixel images at a 1-minute cadence. However, during this observing run at the DST, the images were digitized as 12-bit integers, saved on hard-disk, and later archived on DLT tape for post-processing.

The FOV of the speckle interferometry channel was  $81'' \times 81''$ , which corresponds to an image scale of  $0.08'' \text{ pixel}^{-1}$ . The observations were taken in a green continuum window at 520 nm and the bandpass of the interference was 52 nm. The diffraction limited resolution of the 76 cm DST at 527 nm is defined according to the Rayleigh criterion  $\theta_{\text{Rayleigh}} = 1.22 \cdot \lambda / D = 0.17''$ . However, the Rayleigh criterion is related to the separation of two point sources, so we prefer the stricter criterion  $\theta = \lambda / D = 0.14''$ , which is appropriate when dealing with extended objects and telescopes with circular apertures. Comparing the diffraction limit and image scale indicates that the speckle images are slightly undersampled by about 12%. In order to obtain more reliable information at high spatial frequencies, i.e., to improve the signal-to-noise ratio at these frequencies, the data should have been oversampled by at least 50%. However, this would have restricted the FOV too much for our science program.

A total of 102 sequences of short-exposure images were taken with a 1-minute cadence from 15:28 UT to 17:28 UT, with the exception of a short interruption in the data acquisition from 16:09 UT to 16:27 UT. Each sequence consists of a series of 100 short-exposure images, which were selected from a total of 200 images. The frame selection algorithm is based on the rms-contrast of a distinct solar feature (e.g., Scharmer, 1989), which was in this case a small region of granulation in the North-East corner of the FOV (see Figures 1, 2, 3, and 4) for details. The images were acquired at a rate of  $15 \text{ frames s}^{-1}$ . The first 100 frames are just stored in a

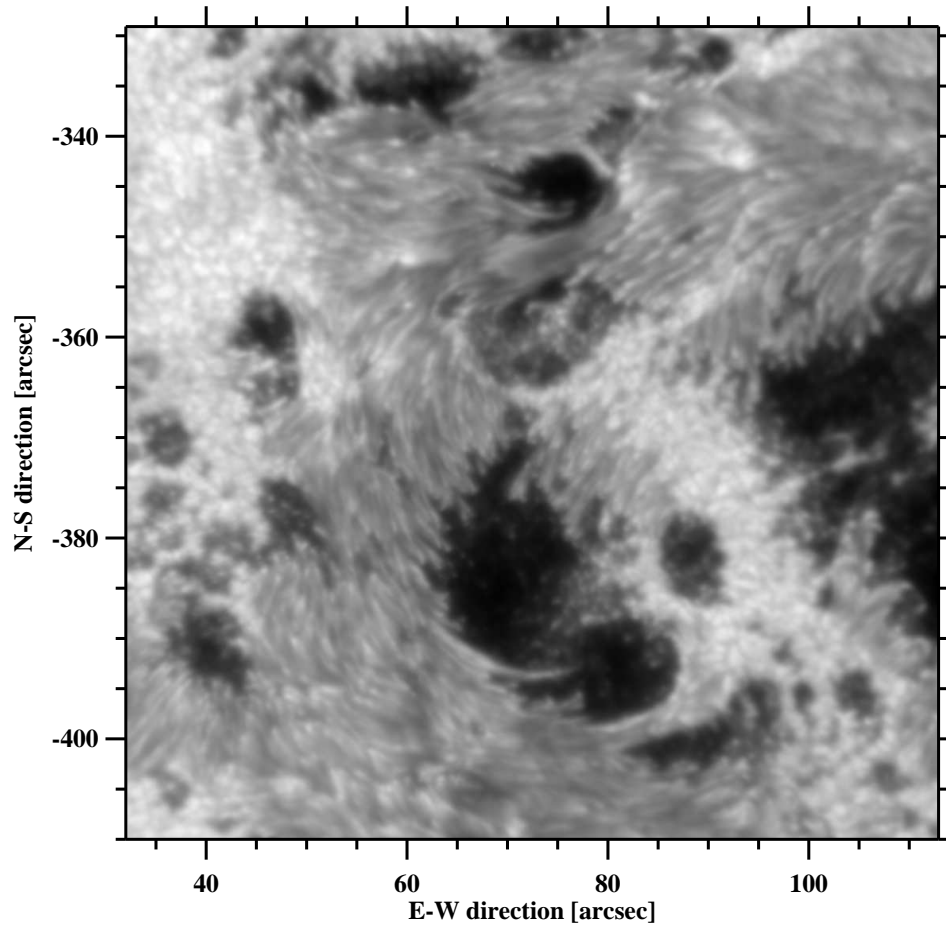


*Figure 1.* Solar active region NOAA 10486 observed at 16:48 UT on 2003 October 29. The “long-exposure” image is the average of 100 short-exposure images captured during a period of about 15 s, which corresponds to an equivalent exposure time of 400 ms – an exposure time that is typically encountered in high-resolution two-dimensional spectroscopy.

stack of 100 pre-allocated memory buffers and the 100 subsequent frames overwrite the image with the lowest rms-contrast only if their rms-contrast is higher. This has the advantage of requiring the smallest amount of memory and overhead for keeping track of rms-contrast values. Since the granulation area used to compute the image contrast was small, the camera operated close to its nominal data acquisition rate, so that individual image sequences were obtained within about 15 s.

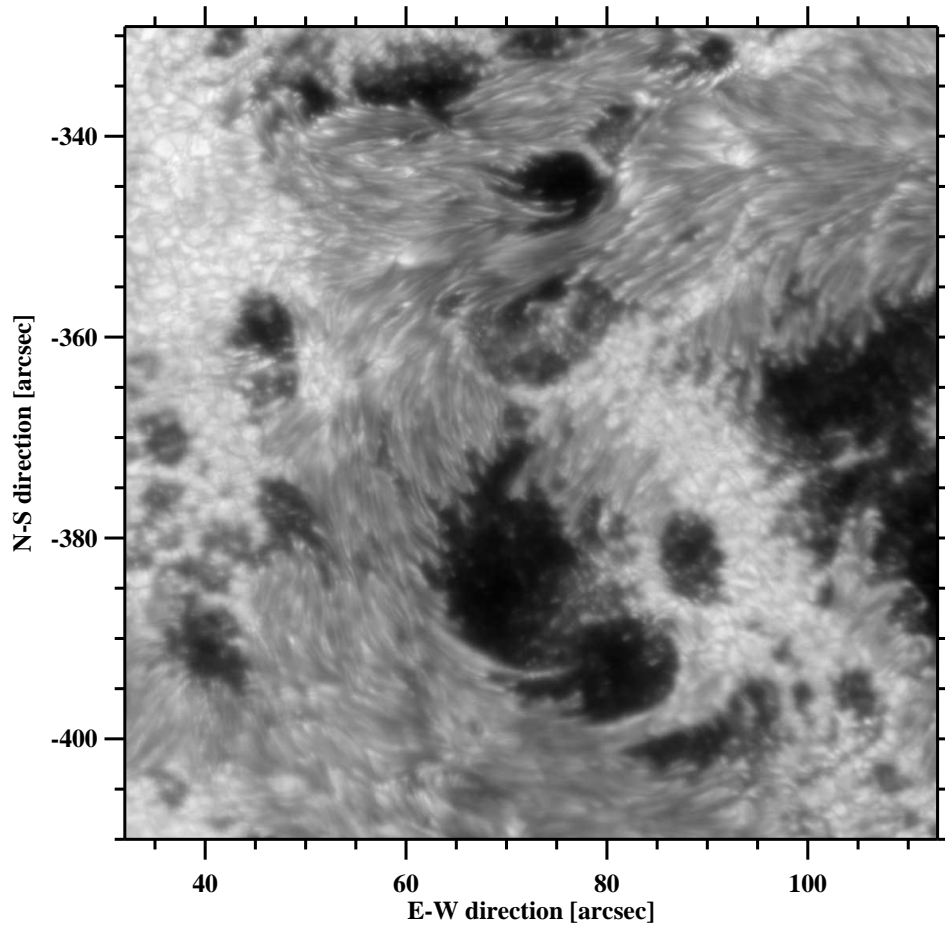


*Figure 2.* The short-exposure “reference” image, which is used in the image reconstruction process to compute image motion and differential image motion, is a frame selected image with the highest granular rms-contrast out of a total of 200 short-exposure images.

#### 4. Image Reconstruction

Speckle masking imaging requires a sequence of short-exposure images each of which is sufficient to “freeze” the wavefront aberrations, which makes it possible to separate the object information and the information on atmospheric turbulence. The exposure time of the specklegrams was 4 ms. The first steps in preprocessing the data concern the usual corrections by means of the average dark and flat field image. The image displacement within the sequence is removed with respect to the image with the highest rms-contrast. Since the short-exposure images were obtained with an AO system, the average image motion should be small and negligible. This was confirmed by computing the average image motion by means of a cross-

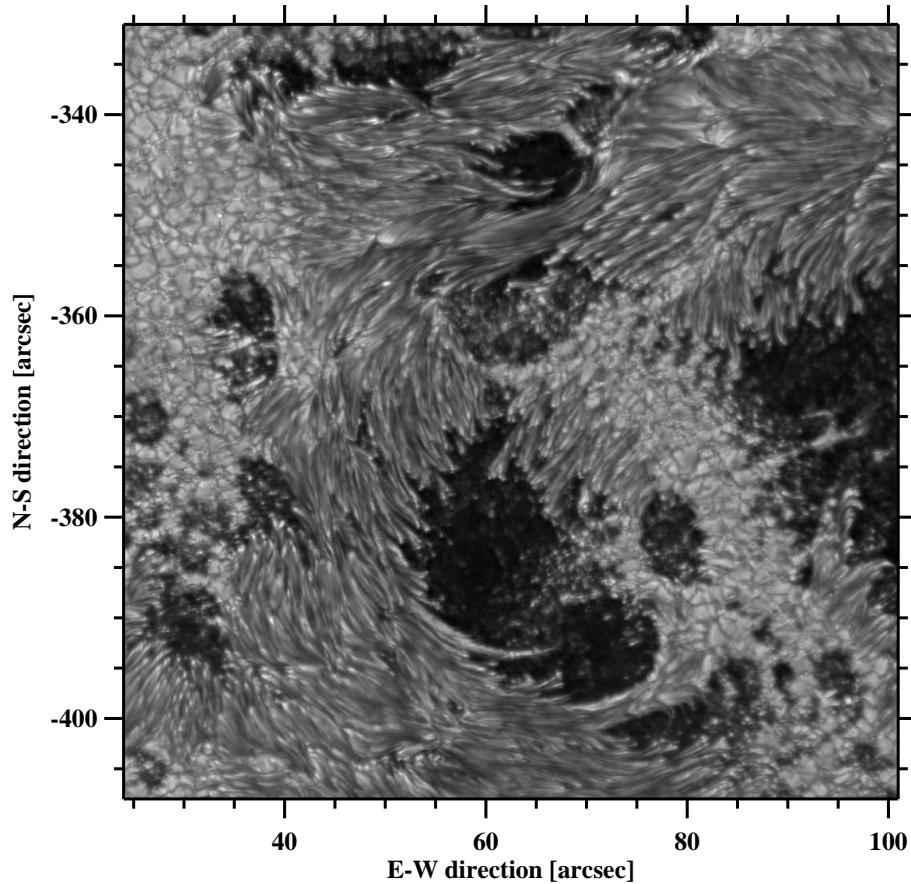


*Figure 3.* Image reconstruction of solar active region NOAA 10486 after high-order AO correction, frame selection, and speckle masking technique have been applied.

correlation analysis with a result of  $0.013''$ . Because this result was of the same order as the inherent errors of the cross-correlation algorithm, it is essentially zero. Since speckle interferometry is only valid for a small region, the isoplanatic patch, the specklegrams have to be divided into mosaics of partially overlapping images. Each isoplanatic patch has a size of approximately  $5.1'' \times 5.1''$ . The differential image displacement in these stacks of  $64 \times 64$  pixel image is also removed.

The time interval between consecutive sequences was approximately 1 min, which is sufficient to study the evolution of solar fine-structures. The typical lifetime of photospheric fine-structures is in the range of 5 to 10 min. The other important time scale for speckle imaging is given by the fact that the object should not change while we take a sequence of short-exposure images. An upper limit for photospheric proper motions is about 2 km/s. Since a typical pixel is about  $0.1''$  or 70 km, the data had to be acquired within about 30 s. In the following sections, when we

use the expression “near real-time imaging”, we refer to a frame rate for speckle interferometry of roughly one speckle reconstruction per minute.

The intensity distribution in the focal plane of a telescope  $i(\vec{x})$  is given by the convolution of the intensity distribution of the object  $i_0(\vec{x})$  and the point spread function (PSF)  $s(\vec{x})$  which describes the atmospheric turbulence along the line-of-sight

$$i(\vec{x}) = i_0(\vec{x}) * s(\vec{x}) \quad . \quad (1)$$

Fourier transformation of Equation 1 yields

$$I(\vec{q}) = I_0(\vec{q})S(\vec{q}) \quad , \quad (2)$$

where the upper case letters denote the Fourier transformation and  $\vec{q}$  is a two-dimensional, normalized spatial frequency. We use the spectral ratio technique to derive the Fried-parameter  $r_0$  (von der L uhe, 1984). Roughly, the Fried parameter corresponds to the aperture of the largest telescope that would just be diffraction limited. The spectral ratio is given by

$$\mathcal{E}(\vec{q}) = \frac{|\langle I(\vec{q}) \rangle|^2}{\langle |I(\vec{q})|^2 \rangle} = \frac{|\langle I_0(\vec{q}) \rangle|^2 |\langle S(\vec{q}) \rangle|^2}{\langle |I_0(\vec{q})|^2 \rangle \langle |S(\vec{q})|^2 \rangle} = \frac{|\langle S(\vec{q}) \rangle|^2}{\langle |S(\vec{q})|^2 \rangle} \quad , \quad (3)$$

where  $\langle \dots \rangle$  denotes an ensemble average. Equation 3 is independent of the object’s intensity distribution and it is only a function of the two average transfer functions  $|\langle S(\vec{q}) \rangle|^2$  and  $\langle |S(\vec{q})|^2 \rangle$ .  $\langle |S(\vec{q})|^2 \rangle$  is the so called speckle transfer function (STF). The observed spectral ratios have been compared with the theoretical values of the STF (Korff, 1973) and the average short-exposure modulation transfer function (MTF, Fried, 1966). The amplitudes of the objects Fourier transform were corrected according to the classical method of Labeyrie (1970)

$$|I_0(\vec{q})|^2 = \frac{\langle |I(\vec{q})|^2 \rangle}{\langle |S(\vec{q})|^2 \rangle} \quad . \quad (4)$$

To derive the phases of the object’s Fourier transform, we use the speckle masking method (Weigelt, 1977; Weigelt and Wirtzner, 1983; Lohmann, Weigelt, and Wirtzner, 1983; de Boer, 1993)

$$\langle I^3(\vec{q}, \vec{p}) \rangle = I_0^3(\vec{q}, \vec{p}) \langle S^3(\vec{q}, \vec{p}) \rangle \quad , \quad (5)$$

where  $I_0^3(\vec{q}, \vec{p}) = I(\vec{q})I(\vec{p})I^*(\vec{q} + \vec{p})$  is the speckle masking bispectrum and  $*$  denotes a conjugate complex quantity,  $\langle S^3(\vec{q}, \vec{p}) \rangle$  is the average speckle masking transfer function (SMTF). The central obscuration of the DST was taken into account computing the STF. However, since the radius of the obscuration is only 10% of the aperture radius, its effect on the STF is negligible. A sensitive noise filter (de Boer, 1996) is applied during the calculation of these phases. Back-transformation of the modulus and phases of the object’s Fourier transform yields a mosaic of partially

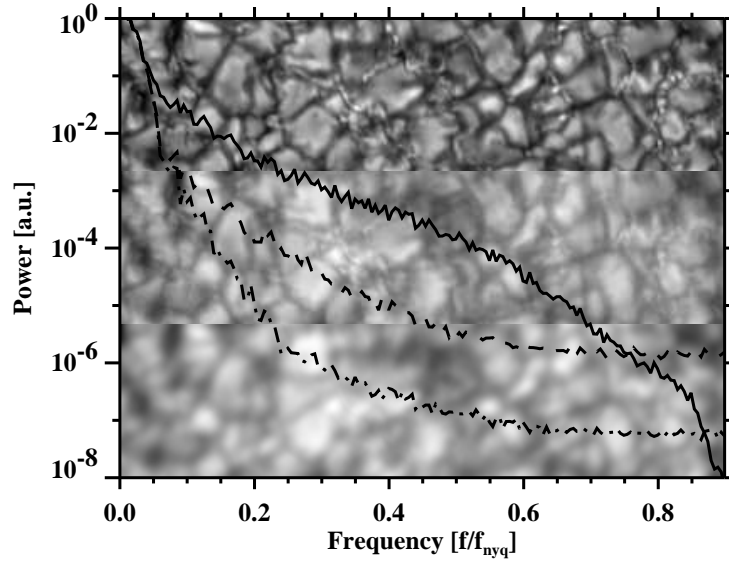


Figure 4. Average power spectra of solar granulation have been obtained from 90 individual, one-dimensional,  $28.5''$ -long intensity profiles for the speckle reconstruction (*solid line*), short-exposure image (*dashed line*), and long-exposure image (*dashed-dotted line*), respectively. The spatial frequencies on the abscissa have been normalized with respect to the Nyquist frequency  $f_{\text{Nyq}}$  and the power values are given in arbitrary units normalized to the first order Fourier component. The three background panels show from top to bottom the same area of granulation in the speckle reconstruction, the short-exposure image, and the long-exposure image. The panels were extracted from the North-East corner of Figures 1, 2, and 3, respectively, and have been rotated counter-clockwise by  $90^\circ$  to fit the aspect ratio of the plotting window. The panels have been independently scaled between maximum and minimum brightness, thus, contrasts are not directly comparable.

overlapping speckle reconstructions. Finally, we align these reconstructions very accurately and assemble the mosaic of isoplanatic patches.

## 5. Results

Figures 1, 2, and 3 illustrate the improvement in image quality that can be achieved by combining high-order AO, frame selection, and speckle masking imaging. Figure 1 is the “long-exposure” image, i.e., the average of 100 short-exposure images corresponding to an effective exposure time of about 400 ms. Exposure times in the range from 100 ms to several seconds are typically encountered in high-resolution two-dimensional spectro-polarimetry, an application where AO systems outperform post-processing techniques, since the latter rely on short exposure times ( $< 40$  ms) to freeze wavefront aberrations. An example of a “short-exposure” image is the frame selected image obtained with an exposure time of 4 ms shown in Figure 2. This “reference” image is used in the image reconstruction procedure to remove image motion and differential image motion. Imaging applications are the domain of

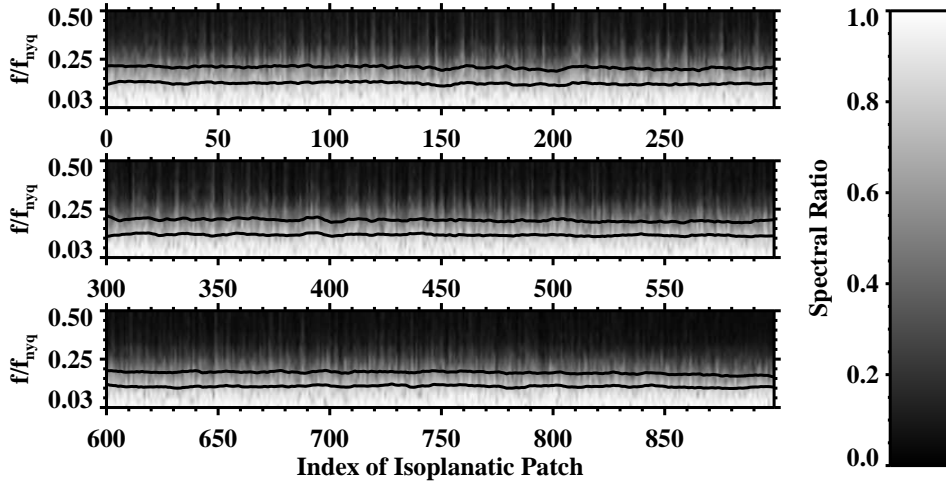


Figure 5. Each speckle reconstruction consists of a mosaic of  $30 \times 30 = 900$  individually reconstructed isoplanatic patches. The azimuthal averages of the spectral ratios are plotted for each isoplanatic patch according to its distance from the AO lock point (see Figure 7). Two black contour lines at the levels  $\mathcal{E}(\vec{q}) = [0.5, 0.3]$  (see Equation 3) were added for clarity.

post-processing techniques, as seen in the improved spatial resolution and contrast of the speckle reconstructed image in Figure 3.

In order to obtain a more quantitative measure of image quality, a region of granulation with  $90 \times 360$  pixel corresponding to  $7.1'' \times 28.5''$  was selected to compute contrasts and power spectra. Note that this region, which is shown as the background image of the power spectra plot in Figure 4, is in the vicinity of the sunspot. It contains filigree and magnetic knots, thus, caution should be taken when comparing contrast and power spectra to quiet sun values. The granular contrasts of the speckle reconstruction, the short-exposure image, and the long-exposure image were 9.3%, 5.1%, and 4.4%, respectively. The granulation was observed at a heliocentric angle of  $\mu = \cos \theta \approx 0.9$  and our contrast values are relatively low compared to other speckle reconstructed observations, e.g., Wilken *et al.* (1997) report granular rms-contrasts, which decrease monotonically from 13.5% at disc center to about 8–9% at  $\mu = 0.1$ . It is to be expected that our contrast is lower by about three percentage points, since the AO system removes much of the image aberrations. Therefore, we overestimate the prevailing seeing conditions and only apply an insufficient correction to the Fourier amplitudes. However, we could achieve the appropriate contrast of about 13.1% by applying a STF that corresponds to a Fried-parameter of 11.9 cm. The image shown in Figure 3 was actually reconstructed with this STF.

The power spectra are averages derived from 90 individual one-dimensional intensity profiles of solar granulation. In Figure 4 and all subsequent plots in the Fourier domain, all frequencies are given in terms of the Nyquist frequency  $f_{\text{nyq}} \approx 9.6 \text{ Mm}^{-1}$ , which was derived from the diffraction limit  $\theta = \lambda/D = 0.14''$ . Zero order terms, which correspond to the image mean, are usually omitted. Since all

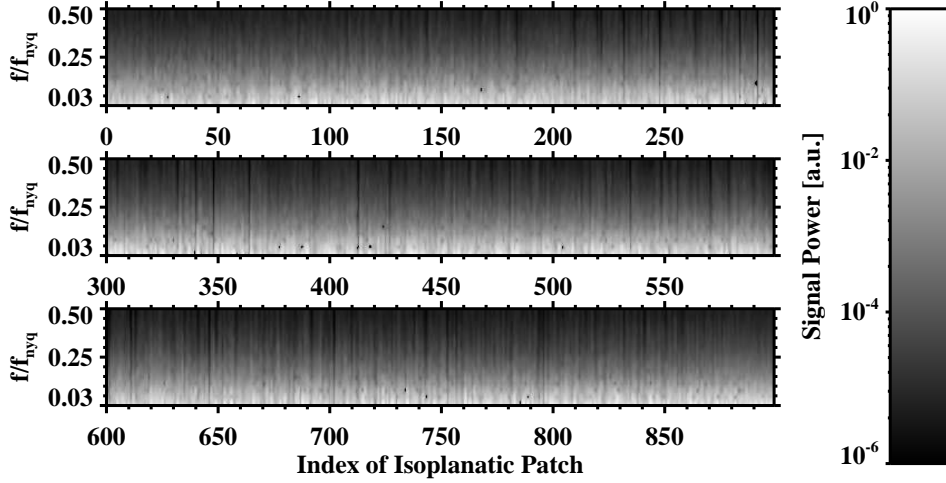


Figure 6. The azimuthal averages of the signal power spectra are plotted for each isoplanatic patch according to its distance from the AO lock point (see Figure 7).

images have a finite size, the lowest frequency in all plots corresponds to image gradients, which has been normalized to unity. The power spectra in Figure 4 are represented by a solid line for the speckle reconstruction, by a dashed line for the short-exposure image, and by a dashed-dotted line for the long-exposure image. The short-exposure power spectrum is basically a scaled version of the long-exposure power spectrum with consistently higher power at all frequencies. The power spectrum of the speckle reconstruction shows systematically higher power values up to a frequency  $f/f_{\text{nyq}} \approx 0.75$ , where it drops below the power spectrum of the short-exposure image. This is a direct result of the optimum and noise filter (de Boer, 1996) that has been conservatively applied in the reconstruction process.

In Figure 5, we show the spectral ratios (see Equation 3) that were computed for each isoplanatic patch ordered by its distance from the lock point of the AO system. Two black contour lines at  $\mathcal{E}(\vec{q}) = [0.5, 0.3]$  were added, clearly showing that the seeing cut-off frequency decreases monotonically with distance from the lock point. This can also be seen in the azimuthal averages of the short-exposure power spectra in Figure 6, which are used as the denominator in the second term from left in Equation 3. In addition, Figure 6 illustrates that signal exists beyond the seeing cut-off frequency in the short-exposure power spectra to be recovered by speckle interferometry. Note that the spectral ratio is an observed quantity. However, the Fried-parameter derived from the spectral ratio relies on models of the transfer functions (Fried, 1966; Korff, 1973). Since both numerator and denominator of the spectral ratio are based on AO corrected images, the Fried-parameter cannot be interpreted in the same way as for uncorrected images. It becomes a measure of image quality with contributions from a diffraction limited point spread function on top of a seeing halo, which could be related to the Strehl ratio. We reluctantly used

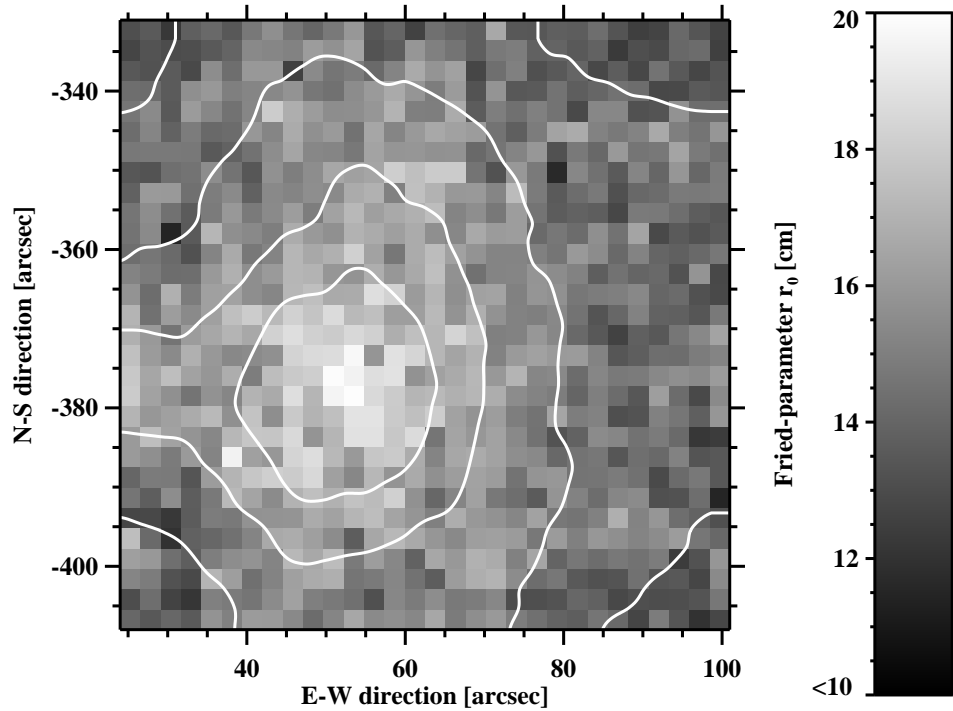
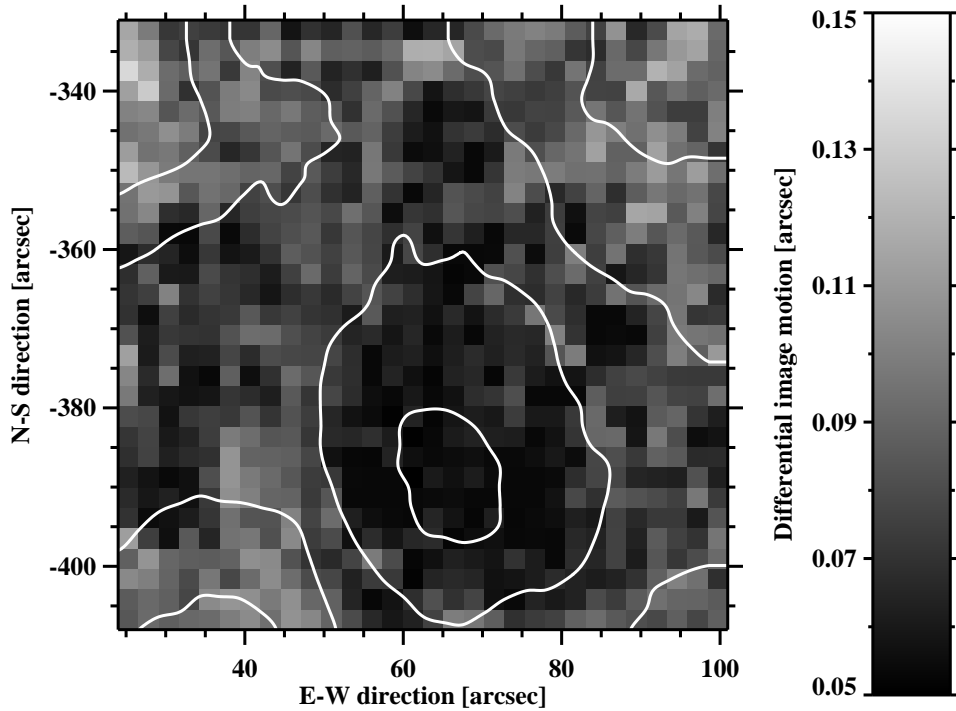


Figure 7. The Fried-parameter  $r_0$  for each isoplanatic patch encoded as a gray scale map. Only the approximate locations of the boxes representing the Fried-parameters are shown, since each reconstructed isoplanatic patch has an overlap of 32 pixel. The white contour lines were derived from a smoothed Fried-parameter map and correspond to  $r_0$ -values of 16.8 cm, 16.0 cm, 15.0 cm, and 14.0 cm, respectively. The lock point of the AO system is approximately located at heliographic coordinate  $52''$  West and  $378''$  South.

the term Fried-parameter in the following sections, since it allowed us to quantify the image correction away from the lock point of the AO system. In the future, we have to develop the theory that will relate the spectral ratio to the Strehl ratio.

Figure 7 provides a graphical representation of the spatial distribution of the measured Fried-parameters  $r_0$  for each of the  $30 \times 30$  isoplanatic patches across the FOV. The overall range of the Fried-parameter ranges from about 10 cm at the periphery of the FOV to 20 cm at the center. An average value  $\bar{r}_0 = 15.6$  cm was used in the reconstruction procedure. The contour lines in Figure 7 were computed from a smoothed image, where we applied a Lee filter algorithm (Lee, 1986) with a nine pixel wide sampling window. The coordinates of the lock point are  $52''$  West and  $378''$  South in heliographic coordinates and were determined by fitting the maximum of the smoothed two-dimensional  $r_0$ -map. The core of the  $r_0$ -map has a roughly circular shape, which fades into a cross-shaped pattern at the periphery of the FOV. This pattern is not an artifact of the smoothing operation but an inherent feature of the AO system. Finally, we can derive the decay of the Fried-parameter



*Figure 8.* Differential image motion for each isoplanatic patch encoded as a gray scale map. The white contour lines were derived from a smoothed differential image motion map and correspond to average patch displacements of  $0.07''$ ,  $0.09''$ ,  $0.11''$ , and  $0.13''$ , respectively. The lock point of the AO system is approximately located at heliographic coordinate  $66''$  West and  $388''$  South. The discrepancy to the  $r_0$  results shown in Figure 7 are explained in the text.

with distance from the AO lock point by a linear fit to the  $r_0$ -values depicted in Figure 7. The average change of the Fried-parameter is  $\Delta r_0 = 1$  cm per  $13''$ .

The previous observations were also confirmed when computing a two-dimensional map of the differential image motion displayed in Figure 8. Even though the AO system efficiently removes image motion, differential image motion between isoplanatic patches remains with a rms-value of one to two pixel in a time sequence of 100 short-exposure images. The graphical representation of the differential image motion in Figure 8 shows the same distinct circular core fading into a cross-shaped pattern. However, the lock point of the AO system appears to be at a different location ( $66''$  West and  $388''$  South),  $17''$  away from the location determined from the  $r_0$ -values. Comparing Figure 8 with Figure 3 provides some insight to explain this discrepancy. Differential image motion is determined by a local cross-correlation analysis, which works best in regions with high signal-to-noise ratio. Here, however, the AO lock point is close to the umbral core of NOAA 10486, thus, shifting the location of the AO lock point to the South-West due to the lower than expected differential image displacements. The case is just the opposite for the computation of

the Fried-parameter. Here, we expect higher values, the more fine structure contents is available, which is the case in regions with granulation and penumbral filaments. Therefore, the  $r_0$ -derived AO lock point is likely shifted to the North-East.

## 6. Discussion and Conclusions

The region of the essential speckle masking signal is proportional to  $\alpha^4 = (r_0/D)^4$  and depends on two distinct and separate terms related to seeing and telescope (see Equation 24 in von der Lühe, 1985)

$$\langle S^3(\vec{q}, \vec{p}) \rangle = \langle S(\vec{q})S(\vec{p})S^*(\vec{q} + \vec{p}) \rangle \cong 0.356\alpha^4 S_0(\vec{q}, \vec{p}) \quad , \quad (6)$$

where  $S_0(\vec{q}, \vec{p})$  depends only on the complex amplitude transmittance of the telescope's entrance pupil. In this region, the SMTF provides unbiased information on the object phases and does not introduce systematic phase terms. The improved Strehl ratio due to the high-order AO system helps the phase recovery, since in this case the signal-to-noise ratio is more important than the signal itself, which is proportional to  $\alpha^4$ , and could be rather low. The approximations used to derive Equation 6 are only valid in a limited range of spatial frequencies ( $\alpha < |\vec{q}|, |\vec{p}|$ , and  $|\vec{q} - \vec{p}| < (1 - \alpha)$ ), but become more accurate with deteriorating seeing or with increasing telescope apertures, i.e., speckle masking imaging becomes an even more important post-processing technique in the context of the 4-meter aperture ATST. Since the Fried-parameter  $r_0$  is proportional to  $\lambda^{6/5}$ , about a factor of four between 500 nm and 1.56  $\mu\text{m}$ ,  $\alpha$  can become large for NIR observations, thus, limiting the range of spatial frequencies. A practical limit for the speckle masking technique is  $\alpha = r_0/D > 0.3$ .

In principle, speckle masking is able to remove telescope aberrations on scales large than the Fried-parameter  $r_0$ . However, the high-order AO system already removes telescope aberrations, which can be distinguished from atmospheric seeing, since they usually occur at low temporal frequencies as can be determined from temporal power spectra of Zernike modes representing the wavefront fluctuations (see Figure 5 in Rimmele, 2000). Even in well designed telescopes, telescope aberrations cannot be neglected, e.g., the entrance windows of vacuum telescopes have been identified as a significant source of wavefront aberrations. In any case, the high-order AO system ensures that the effects of atmospheric seeing surmount the telescope aberrations, thus, supporting even stronger the assumptions inherent to the derivation of Equation 6. As long as the recovery of Fourier phases is concerned, AO correction of telescope aberrations actually enforces the underlying theory of speckle masking.

According to Moore's law of exponential growth in computing power, we can expect an increase of computing power by a factor of 16 over the next six years which will allow us to operate  $2,048 \times 2,048$  pixel or even larger CCD cameras for speckle interferometry. This will be right in time for the next generation of 2 to

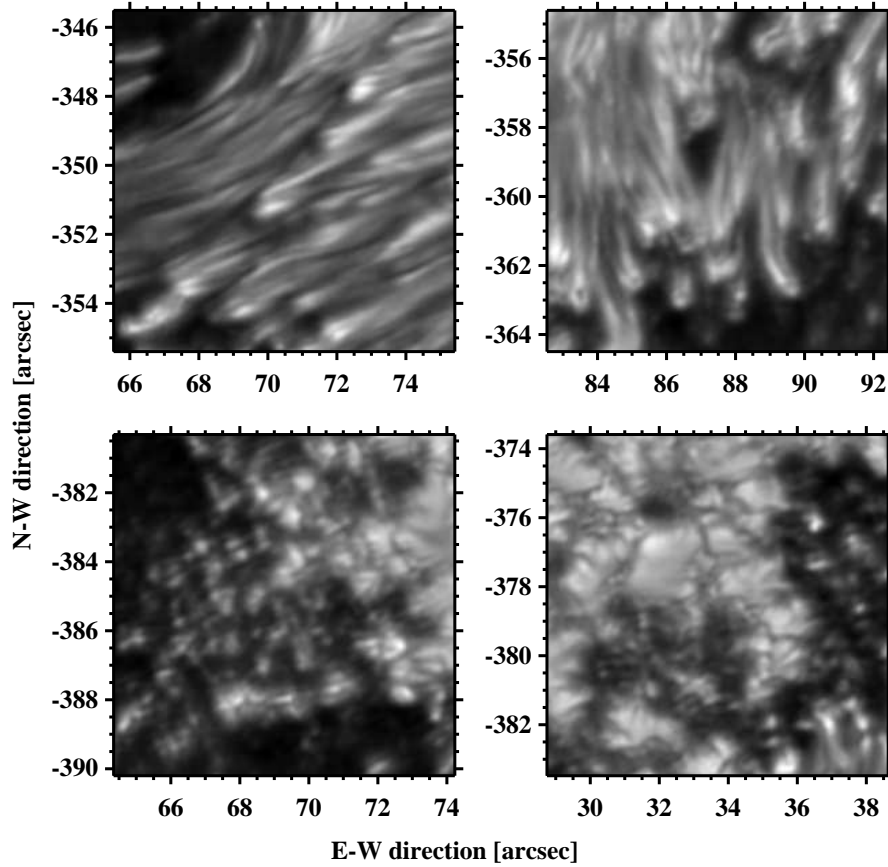


Figure 9. Detailed views of small-scale features shown in Figure 3: (*top-left*) dark cores inside umbral filaments, (*top-right*) internal dark structures in penumbral grains, (*bottom-left*) densely packed umbral dots, and (*bottom-right*) magnetic knots, filigree, and pores.

4 meter-class telescopes, which will provide diffraction limited observations with a spatial resolution of better than  $0.05''$  at 500 nm with a FOV of about  $100'' \times 100''$ , sufficiently large to cover sunspots and substantial parts of active regions. The data rate for such a system is expected to be in excess of one GByte per minute. We are certain that large format, high frame rate CCD cameras for speckle interferometry or other post-processing techniques in combination with parallel computers will become standard post-focus instruments for advanced solar telescopes. Real-time image reconstruction (Denker, Yang, and Wang, 2001) will not only aid our basic scientific understanding of solar activity but also enhance space weather forecast and prediction capabilities. The visualization of photospheric flow fields in solar active regions with the highest possible spatial and temporal resolution is extremely

important in predicting solar flares, filament eruptions and disappearances, as well as coronal mass ejections (CMEs).

Finally, we would like to high-light with Figure 9 some of the science that will be addressed in upcoming papers. Xu *et al.* (2004) present high-resolution of an NIR X10 white-light flare, We will use the speckle reconstructed time series to study changes in the pre-flare state of active region NOAA 10486 and search for flow pattern that are related to the strong magnetic shear observed in NOAA 10486. The top row shows two features, dark cores inside umbral filaments and internal dark structures in penumbral grains, that were first reported by Scharmer *et al.* (2002). Since our multi-faceted image reconstruction approach is quite different, we are ascertained that these features are real. The bottom row of Figure 9 shows a region of densely packed umbral dots, which exhibit a striking similarity to magnetic knots, filigree, and pores observed near the eastern edge of the speckle reconstruction.

### Acknowledgements

This work was supported by NSF under grant ATM 00-86999, ATM 02-36945, IIS ITR 03-24816 and AST MRI 00-79482 and by NASA under grant NAG 5-12782. Dulce Mascarinas has been supported through a summer research for undergraduates stipend of the New Jersey Space Grant Consortium. We would like to thank Drs. Franz Kneer and Claus-Rüdiger de Boer (Universitäts-Sternwarte Göttingen) for providing the original version of the IDL speckle masking algorithms. Obtaining the excellent data would not have been possible without the help of the dedicated observing staff at the Dunn Solar Telescope. The National Solar Observatory/Sacramento Peak is a Division of the National Optical Astronomy Observatories, which is operated by the Association of Universities for Research in Astronomy, Inc., under cooperative agreement with the National Science Foundation.

### References

- de Boer, C. R., 1993: *Speckle-Interferometrie und ihre Anwendung auf die Sonnenbeobachtung*, Ph.D. Thesis, Georg-August Universität Göttingen, Germany.
- de Boer, C. R., 1996: 'Noise Filtering in Solar Speckle Masking Reconstructions', *Astron. Astrophys. Suppl. Ser.* **120**, 195.
- Denker, C., Yang, G., and Wang, H., 2001, 'Near Real-Time Image Reconstruction', *Sol. Phys.* **202**, 63.
- Didkovsky, L. V., Dolgushyn, A., Marquette, W. H., Nenow, J., Varsik, J., Goode, P. R., Hegwer, S. L., Ren, D., Fletcher, S., Richards, K., Rimmele, T., Denker, C., and Wang, H., 2003: 'High-Order Adaptive Optical System for Big Bear Solar Observatory', *Proc. SPIE* **4853**, 630.
- Fried, D. L., 1966: 'Optical Resolution Through a Randomly Inhomogeneous Medium for Very Long and Very Short Exposures', *J. Opt. Soc. Am.* **56**, 1372.

- Goode, P. R., Denker, C., Didkovsky, L. I., Kuhn, J. R., and Wang, H., 2003: '1.6-Meter Solar Telescope in Big Bear – The NST', *J. Korean Astron. Soc.* **36**, 125.
- Keil, S. L., Rimmele, T., Keller, C. U., Hill, F., Radick, R. R., Oschmann, J. M., Warner, M., Dalrymple, N. E., Briggs, J., Hegwer, S. L., and Ren, D., 2003: 'Design and Development of the Advanced Technology Solar Telescope (ATST)', *Proc. SPIE* **4853**, 240.
- Korff, D., 1973: 'Analysis of a Method for Obtaining Near-Diffraction-Limited Information in the Presence of Atmospheric Turbulence', *J. Opt. Soc. Am.* **63**, 971.
- Labeyrie, A., 1970: 'Attainment of Diffraction Limited Resolution in Large Telescopes by Fourier Analyzing Speckle Patterns in Star Images', *Astron. Astrophys.* **6**, 85.
- Langlois, M., Rimmele, T. R., and Moretto, G., 2004: 'Three-Dimensional High-Order Wavefront Sensing, Anisoplanatism, and Evaluation of the Feasibility of Solar MCAO', *Proc. SPIE* **5171**, 187.
- Lee, J.-S., 1986: *Opt. Eng.* **25(5)**, 636.
- Lohmann, A. W., Weigelt, G. P., and Wirtitzer, B., 1983: *Appl. Opt.* **22**, 4028.
- Ren, D., Hegwer, S., Rimmele, T., Didkovsky, L., and P. R., Goode, 2003: 'The Optical Design of a High Order Adaptive Optics System for the NSO Dunn Solar Telescope and the Big Bear Solar Observatory', *Proc. SPIE* **4853**, 593.
- Richards, K., Rimmele, T. R., Hill, R., and Chen, J., 2004: 'High Speed Low Latency Solar Adaptive Optics Camera', *Proc. SPIE* **5171**, 316.
- Rimmele, T., 2000: 'Solar Adaptive Optics', *Proc. SPIE* **4007**, 218.
- Rimmele, T. R., Richards, K., Hegwer, S. L., Ren, D., Fletcher, S., Gregory, S., Didkovsky, L. V., Denker, C., Marquette, W., Marino, J., and Goode, P. R., 2003: 'Solar Adaptive Optics: A Progress Report', *Proc. SPIE* **4839**, 635.
- Scharmer, G. B., 1989: 'High Resolution Granular Observations from La Palme: Technique and First Results', *NATO ASI Ser.* **263**, 161.
- Scharmer, G. B., Gudiksen, B. V., Kiselman, D., Löfdahl, M. G., and Rouppe van der Voort, L. H. M., 2002: 'Dark Cores in Sunspot Penumbra Filaments', *Nature* **420**, 151.
- Scharmer, G. B., Bjelksjö, K., Korhonen, T. K., Lindberg, B., and Petterson, B., 2003: 'The 1-Meter Swedish Solar Telescope', *Proc. SPIE* **4853**, 341.
- Volkmer, R., von der Lühse, O., Kneer, F., Staude, J., Hofmann, A., Schmidt, W., Sobotka, M., Soltau, D., Wiehr, E., Wittmann, A., and Berkefeld, T., 2003: 'GREGOR: The New 1.5-Meter Solar Telescope on Tenerife', *Proc. SPIE* **4853**, 360.
- von der Lühse, O., 1984: 'Estimating Fried's Parameter from a Time Series of an Arbitrary Resolved Object Imaged Through Atmospheric Turbulence', *J. Opt. Soc. Am. A* **1**, 510.
- von der Lühse, O., 1985: 'The Speckle Masking Transfer Function', *Astron. Astrophys.* **150**, 229.
- Weigelt, G. P., 1977: 'Modified Astronomical Speckle Interferometry – Speckle Masking', *Opt. Comm.* **21**, 55.
- Weigelt, G. and Wirtitzer, B., 1983: 'Image Reconstruction by the Speckle Masking Method', *Opt. Lett.* **8**, 389.
- Wilken, V., de Boer, C. R., Denker, C., and Kneer, F., 1997: 'Speckle Measurements of the Centre-to-Limb Variation of the Solar Granulation', *Astron. Astrophys.* **325**, 819.
- Xu, Y., Cao, W., Liu, C., Yang, G., Jing, J., Denker, C., and Wang, H., 2004: 'Study of the 2003 October 29 X10 White-Light Flare Observed at 1.56  $\mu\text{m}$ ', *Astrophys. J.*, in preparation.